Korean J. Chem. Eng., 39(4), 920-927 (2022)
DOI: 10.1007/s11814-021-1001-3

pISSN: 0256-1115
eISSN: 1975-7220

The effect of Zn doping on active Cu species and its location of Cu-exchanged mordenite for the stepwise oxidation of methane to methanol

Nutchapon Chotigkrai*,†, Phakpum Tannititam*, Sunthon Piticharoenphun*, Narit Triamnak, Supareak Praserthdam***,****, and Piyasan Praserthdam***,****

*Department of Chemical Engineering, Faculty of Engineering and Industrial Technology, Silpakorn University, Nakhon Pathom, Thailand 73000
**Department of Materials Science and Engineering, Faculty of Engineering and Industrial Technology, Silpakorn University, Nakhon Pathom, Thailand 73000
***Department of Chemical Engineering, Faculty of Engineering, Chulalongkorn University, Bangkok, Thailand 10310
****Center of Excellence on Catalysis and Catalytic Reaction Engineering, Chulalongkorn University, Bangkok, Thailand 10330

(*Received 2 August 2021 • Revised 24 October 2021 • Accepted 31 October 2021*)

Abstract−The effect of Zn doping (0.5-3 wt%) on Cu-exchanged mordenite (Cu-MOR) was investigated during the stepwise oxidation of methane to methanol. The strong interaction between Cu and ZnO_x stabilized the highly-dispersed state of Cu^{2+} but reduced the Cu^{2+} bounded to extra-framework oxygen (active site), as demonstrated by the H_2-TPR and XPS results. The Cu/Al and Zn/Al ratios suggested that Zn preferably bonded to the sites in the 8-MR channel, which led to highly dispersed Cu^{2+} anchored onto the highly accessible sites (12-MR and 8-MR side pocket). The reactivity indicated that highly dispersed Cu^{2+} can be gradually transformed into active Cu^{2+} species during contact with methane. Bimetallic Cu-ZnO_x was also able to activate methane, resulting in a product complex. Although Zn-doped Cu-MOR catalysts gave a lower methanol yield at 2 h, a higher methanol yield could be achieved at saturation methane loading time. Interestingly, 3 wt% Zn doping on Cu-MOR showed superior activity due to the increase of methanol yield up to 20% at 5 h of methane loading time. This work paves the way for the design of highly dispersed Cu^{2+} in the 12-MR channel of mordenite zeolite via the control of strong Cu-ZnO_x interaction.

Keywords: Copper-zinc, Highly Dispersed Copper(II), Copper Mordenite, Copper Reduction, Methane to Methanol

INTRODUCTION

Methane is an abundant compound as it is a major component of several natural resources such as natural gas, shale gas, methane hydrate, and biogas obtained from wastewater from various industrial plants and ranches [1,2]. However, methane is only used as heating fuel or flaring at remote sites because of the high cost of gas transport [2]. Therefore, the conversion of methane into other higher-value products has widely gained attention. Methanol is one of the preferable high-value products obtained from the conversion of methane, because it can be broadly used as derivatives such as solvents, a precursor of high-quality fuel, additives, olefins [3]. In addition, methanol is more favorable in terms of its economical transport compared to methane. Because of the highly stable C-H bond of methane, the commercial technology of methanol synthesis from methane is based on energy-extensive indirect processes, such as syngas production at high temperature (~800 °C) and high pressure (~50 bar). However, this process can only be used in large-scale plants for economic feasibility [4]. Thus, an efficient process for converting methane into methanol in mild conditions is a great challenge for methane valorization, especially for remote areas and small-scale plants.

Methane can be directly converted into methanol in mild conditions with gas-phase continuous and liquid-phase batch processes. However, the drawback is low selectivity because of the higher reactivity of methanol compared to methane [5]. Interestingly, it was found that a natural catalyst, methane monooxygenase enzymes (MMO), can convert methane into methanol in water with high selectivity at ambient temperature and pressure. This discovery was explained with the function of di-copper [6] and di-iron [7] as active sites. Hence, many efforts have been put into mimicking the enzyme active sites on other more stable materials such as metal oxides. Due to the confinement of zeolite, direct stepwise conversion of methane into methanol at mild conditions over Cu-containing ZSM-5, introduced by Groothaert et al. [8], showed interestingly high selectivity. Generally, the stepwise manner (cyclic process) includes three sequential steps: activation of O_2 at high temperature (~450 °C), loading of CH_4 at a lower temperature (~200 °C), and off-line methanol extraction in liquid water. Lately, the third step was modified to be online extraction by using vapor steam to extract methanol in the reactor after methane loading. The third step modification yields higher effectiveness, leading to a higher production rate because of its simpler operation [9]. Moreover, Román-Leshkov's group [10] demonstrated the possibility of continuous conversion by flow-

†To whom correspondence should be addressed.
E-mail: chotigkrai_n@silpakorn.edu

ing the stream of CH_4, O_2, and H_2O simultaneously at 210 °C over Cu-ZSM-5, producing methanol with selectivity as high as 70%, approximately. Other zeolites such as mordenite, chabazite, and mazzite have been studied for the cyclic process. One of the most studied and superior catalysts is Cu-exchanged H-form mordenite (Cu-MOR) [11]. However, the production rate is still far too low for industrial applications. To develop the Cu-MOR toward industrial viability, the increase of the methanol yield is crucial for both cyclic and continuous processes, and it can be achieved by increasing the active site density. The addition of second metals has been widely applied to improve those properties for supported metal catalysts [12,13]. However, for this stepwise reaction, most studies use monometallic copper-zeolites, which are based on different topologies and material compositions. Only a few works have studied bimetallic Cu-based zeolites such as Cu-Pt and Cu-Pd [14]. Among the bimetallic catalysts, Cu-Zn supported on SiO_2 has been applied in numerous reactions such as ethylene glycol synthesis, methanol synthesis [15-18]. This is due to the strong interaction between Cu and Zn, promoting the high dispersion of Cu and sintering resistance [17,18]. Moreover, Reule et al. [19] reported that the addition of Zn into Cu-exchanged mordenite zeolite resulted in stabilizing high Cu dispersion in carbonylation reactions. Gabrienko et al. [20] also demonstrated that Zn-exchanged ZSM-5 zeolites could activate methane towards methyl species at low temperature and even at room temperature. In addition, the creation of methoxy species (methanol precursor) at the Zn active sites by flowing O_2 after the methyl species was formed. This suggested that Zn could be a promising promoter of Cu-exchanged mordenite for enhancing active site density and methane activation.

In this study, we report the promotional effect of Zn on Cu-exchanged MOR catalysts (Cu-MOR) for the stepwise oxidation of methane into methanol. Zn was doped on Cu-MOR catalysts by incipient wetness impregnation. The prepared catalysts were characterized using XRD, N_2-physisorption, ICP-OES, H_2-TPR, and XPS.

EXPERIMENTAL

1. Catalyst Preparation

H-form mordenite zeolite (Si/Al=9) was purchased from Tosoh Chemical. Copper (II) acetate monohydrate (98%) and zinc (II) nitrate hexahydrate (98%) were purchased from Sigma-Aldrich. Copper-exchanged mordenite catalyst was prepared by the ion-exchange method. Mordenite (10 g) was stirred in aqueous solutions of copper (II) acetate monohydrate (0.01 M, 780 mL) at room temperature for 24 h. The suspension was then filtered at room temperature using a vacuum pump. The ion-exchange step was repeated twice. Next, the suspension was dried overnight at 120 °C in an oven and then calcined at 500 °C for 5 h with a heating rate of 3 °C/min, denoted as Cu-MOR (reference catalyst). For Zn doped on Cu-MOR catalyst, 3 g of Cu-MOR was impregnated with the aqueous solution of zinc (II) nitrate hexahydrate, using the Zn concentration of 0.5, 1, and 3 wt% on a dry basis. The Zn doped on Cu-MOR catalyst was denoted as xZn/Cu-MOR, where x is a weight percent of Zn. All the final catalysts were left in ambient conditions for 1 h, dried overnight at 120 °C in an oven, and calcined in dry air at 500 °C for 5 h with a heating rate of 3 °C/min. The catalyst with 3 wt% Zn supported on mordenite was also prepared by incipient wetness impregnation and was assigned to 3Zn/MOR.

2. Catalyst Characterization

The crystallinity of mordenite zeolite and Cu-containing catalysts was investigated by XRD technique using a Shimadzu (LabX XRD-6100) X-ray diffractometer. The XRD patterns of the samples were measured in the range of 10° to 70°. N_2-physisorption (BELSORP-mini II) was used to determine the pore structure and specific surface area of the catalysts. The catalysts were degassed at 180 °C for 3 h. The BET surface area and micropore volume were determined from the amount of N_2 adsorbed at P/P_0=0.02. The elemental composition of catalysts was determined using inductively coupled plasma-optical emission spectrometry (ICP-OES, Agilent 710 series). Before ICP-OES measurement, the catalyst was digested with 1.2 M HCl. The reducibility of catalysts was examined using temperature-programmed reduction in H_2 (H_2-TPR) (Micromeritics Auto Chem 2910 instrument/thermal conductivity detector). 100 mg catalyst was placed in a quartz U-tube reactor. The catalyst was activated in O_2 flow (30 mL/min) at 550 °C for 5 h. The reducibility profile from 100-800 °C was conducted in 10% H_2/N_2 flow (30 mL/min) with a ramp rate of 10 °C/min. The generated water was trapped in a cold alcohol bath before entering the detector. The consumption of H_2 was calibrated using the CuO sample as a reference at similar conditions. The oxidation states of Cu and Zn species were determined by X-ray photoelectron spectroscopy (XPS). XPS was performed on a Kratos AMICUS X-ray photoelectron spectrometer using MgK_α as X-ray radiation. The C 1s (284.6 eV) and Si 2p (103.4 eV) were specified as multiple internal standards. After background subtraction using the Shirley approach, the Cu $2p_{3/2}$, and Zn $2p_{3/2}$ peaks were fitted using Gaussian peaks. Cu/Al molar ratio was calculated by normalizing areas of the spectra to relative sensitivity factors (RSF). The sample was pretreated in O_2 flow at 550 °C for 5 h and quickly transferred to a sealed vial just before the XPS experiment was performed.

3. Stepwise Oxidation of Methane into Methanol

The stepwise reaction was carried out in a tubular flow reactor (quartz tube, O.D. 12.7 mm) at ambient pressure. 1 g catalyst was packed between two quartz wool layers at the center of the reactor tube, which was mounted inside a furnace. First, the catalyst was activated in O_2 flow (30 mL/min) at 550 °C for 5 h with a heating rate of 3 °C/min and then cooled to the reaction temperature (200 °C). Then, O_2 was flushed with argon (30 mL/min) for 15 min before being switched with methane (50 mL/min) for different durations. After that, the methane was flushed with argon (30 mL/min) for 15 min and cooled to ambient temperature. The catalyst was unpacked, stirred in deionized water (5 mL) for 24 h, and filtered. Acetonitrile was added to the extracted solution (5% V/V) as an external standard. The residual solid was filtered using a syringe filter. The product solution was analyzed using gas chromatography (GC) equipped with a flame ionization detector (FID). Methanol yield was calculated by an average of five injections. The methanol yields of Cu-MOR and 3Zn/Cu-MOR at 5 h were performed in duplicate.

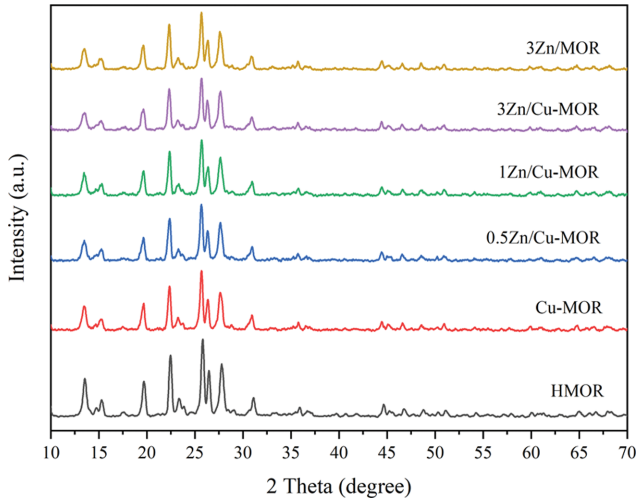

Fig. 1. XRD patterns of catalysts.

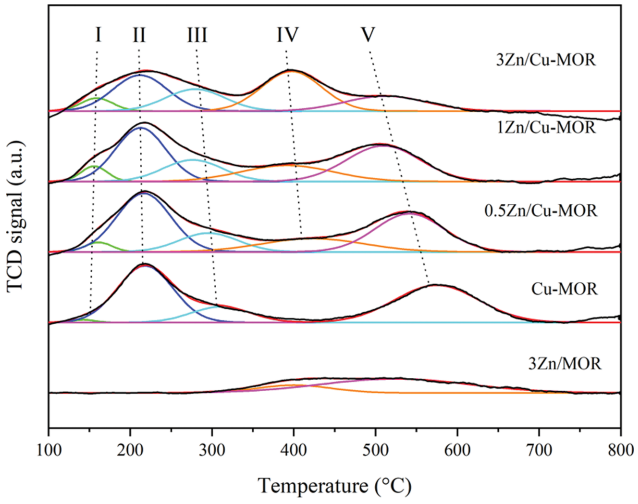

Fig. 2. H_2-TPR profiles of catalysts.

RESULTS AND DISCUSSION

1. Catalyst Characterization

1-1. Physical Properties

XRD patterns of catalysts are shown in Fig. 1. H-form mordenite zeolite (HMOR) revealed intense peaks between 10° and 54°, corresponding to the primary diffraction peaks of the MOR pattern [21,22]. Cu-exchanged mordenite catalysts (Cu-MOR) showed similar patterns with the parent mordenite, indicating that the ion-exchange of Cu into mordenite and calcination did not substantially alter the crystalline structure of mordenite zeolite. Moreover, the XRD peaks of crystalline copper oxide at 35.6° and 38.7° [23], and zinc oxide at 36.5° and 56.5° [24] could not be observed in all samples. It might confirm that incorporation of Cu by ion-exchange and Zn by incipient wetness impregnation provided well-dispersed Cu and/or Zn species on the mordenite surface (smaller than 3 nm). Elemental composition and N_2-physisorption results of catalysts are summarized in Table 1. ICP-OES investigation revealed the result of Cu-MOR with Cu=2.38 wt%, Si/Al=9.4, and Cu/Al=0.24. These values are in agreement with works using copper acetate and Si/Al close to 9 [21]. The Zn concentration of 0.5, 1, and 3Zn/Cu-MOR was 0.58, 1.07, and 3.01 wt% (Zn/Al=0.07, 0.13, and 0.36, respectively) while the Cu concentration was 2.31, 2.18, and 2.20 wt%, respectively. The weight percent of Cu slightly decreased as the amount of Zn increased. However, the Cu/Al molar ratio was nearly similar to 0.24, indicating a small dilution when increasing Zn. The Si/Al for all samples was about 9.0, matching our mordenite specification.

The BET surface area of Cu-MOR was 387 m^2/g and slightly decreased to 378, 377, and 337 m^2/g for 0.5, 1 and 3Zn/Cu-MOR, respectively. The micropore volume of Cu-MOR was 0.17 cm^3/g and remained unchanged except at the highest Zn loading as it slightly reduced to 0.15 cm^3/g, corresponding to the values reported by Narsimhan et al. [25]. The small decrease of BET surface area at higher metal loading is typical and can be explained by pore filling and the partial pore blockage of mordenite zeolite by incorporated metal [21,26]. The results strongly suggest that the addition of Zn and double calcination did not destroy the crystalline structure of mordenite zeolite. This highlights the influence of Zn on active Cu species and their locations for stepwise oxidation of methane into methanol.

1-2. H_2-temperature Programmed Reduction

Fig. 2 represents the H_2-TPR profiles of the catalysts in this study. The profile of Cu-MOR exhibits two broad regions, centered at 218 and 575 °C with H_2 uptake of 193.8 and 146.0 μmol/g-cat., respectively. The total H_2 consumption was 339.8 μmol/g-cat., resulting in the H_2/Cu molar ratio of 0.91 for Cu-MOR (Cu=2.38 wt%). Theoretically, the stoichiometric reduction ratio of Cu^{2+} and Cu^{+} to Cu^0 is 1 and 0.5, respectively. Hence, the H_2/Cu molar ratio of 0.91 suggests that the sample could include the portion of Cu^{+} even after the activation in O_2 at 550 °C. Furthermore, the concentration of Cu^{2+} and Cu^{+} was determined to be 81 and 19%, approxi-

Table 1. Elemental composition and N_2-physisorption analysis of catalysts

Catalyst	Elemental composition					BET surface area (m^2/g-cat.)	Micropore volume (cm^3/g-cat.)
	Cu (wt%)	Zn (wt%)	Cu/Al	Zn/Al	Si/Al		
Cu-MOR	2.38	-	0.24	-	9.4	387	0.17
0.5Zn/Cu-MOR	2.31	0.58	0.25	0.07	9.2	378	0.17
1Zn/Cu-MOR	2.18	1.07	0.24	0.13	9.0	377	0.17
3Zn/Cu-MOR	2.20	3.01	0.24	0.36	9.0	337	0.15
3Zn/MOR	-	3.39	-	0.38	8.9	378	0.17

Table 2. Reduction peak and H_2 consumption of the fitting H_2-TPR measurement

Catalyst	Reduction peak (°C)					H_2 consumption (μmol/g-cat.)					
	I	II	III	IV	V	I	II	III	IV	V	Total
Cu-MOR	144	218	311	-	575	2.8	147.5	43.5	-	146.0	339.8
0.5Zn/Cu-MOR	161	217	296	423	541	12.1	148.8	52.5	64.8	123.8	402.0
1Zn/Cu-MOR	156	213	277	392	510	18.9	126.4	60.0	69.5	123.6	398.4
3Zn/Cu-MOR	159	212	279	397	512	19.2	90.9	60.6	111.4	56.6	338.7
3Zn/MOR	-	-	-	400	524	-	-	-	27.3	98.4	125.7

mately. The two broad regions mentioned above are typically attributed to the reduction of Cu active sites at different locations of MOR zeolite. The low-temperature range (218 °C) was referred to as the highly accessible sites such as those on the external surface and in the largest pore (12-MR), while the high-temperature range (575 °C) was designated to the less accessible sites in the 8-MR pore [21,27].

To gain more details on the active Cu species, the H_2-TPR profiles were deconvoluted and summarized in Table 2 (quantitative data). The fitting of the Cu-MOR result shows three peaks, centered at 144, 218, and 311 °C. The peak below 200 °C (peak I) corresponds to the reduction of CuO or small clusters of Cu_2O at the external surface. The peak at 218 °C (peak II) is ascribed to the reduction of Cu^{2+} in the largest pore (12-MR), while the peak at 311 °C (peak III) is assigned to the sites in the 8-MR side pocket [28]. The framework-oxygen that was neutralized by Cu cations could be neutralized by protons formed during the reduction as indicated by the appearance of Si-OH-Al vibrations in the NIR spectrum [29]. Without Cu, 3Zn/MOR sample shows a small broad peak from 300-700 °C, approximately, which fits into two peaks at 400 °C and 524 °C. The peak at 400 °C can be attributed to very small ZnO particles [30,31]. However, the peak at 524 °C does not match with either large ZnO particles or bulk ZnO, which usually exhibit a reduction peak above 600 °C [32]. Gong et al. [24] found that the reduction peak at 520 °C corresponded to the isolated $Zn(OH)^+$ species, anchored to the ZSM-5. These species, which are the predominant form of ZnO clusters, were confirmed using the XPS spectra at 1,022.4 eV. Therefore, the peak at 524 °C of Zn/MOR is probably the isolated $Zn(OH)^+$ species.

In the case of the Zn/Cu-MOR samples series, the areas of peaks I and III increased while the area of peak II decreased with increasing Zn loading. These results indicate that the addition of Zn promoted partial transferring of CuO from the main channel to the external surface and 8-MR side pocket. In addition, the increase of the area of peak III may also be due to the strong interaction between Cu species and ZnO, anchored in the main channel, which was confirmed by the reduction peak observation around 290-300 °C in Cu-Zn supported on the SiO_2 sample [16,18]. Peak IV appeared, and the peak area increased along with the decrease of the area of peak V, as well as shifting to a lower temperature, from 575 to 512 °C, due to the increase of Zn loading. Even though peak IV could represent the reduction of very small ZnO particles, it was also influenced by another mechanism confirmed by higher H_2 consumption than 3Zn/Cu-MOR. The increase of peak IV area was clear evidence of the close contact between Cu and very small ZnO particles. This species could be the layer of ZnO_x on Cu, similar to that found in industrial $Cu/ZnO/Al_2O_3$ catalysts [33]. This species has been reported to limit the growth of CuO_x in many works [33,34]. However, this species on metal oxides supports exhibited peaks below 300 °C. It was also reported that peak IV could be explained by the shift of Cu reduction to a higher temperature of Cu/MOR from 250 to 290 and 390 °C when Zn/Cu increased [27]. Moreover, their TEM images confirmed that the presence of Zn could improve Cu dispersion and stability. Therefore, we speculated that peak IV also represented a strong interaction of Cu with ZnO_x located at less-accessible sites such as 8-MR side pockets. On the other hand, Le et al. [21] reported that the peak at high temperatures of Cu-exchanged mordenite obviously shifted to higher temperatures with an increase in O_2 activation temperature due to the enhanced diffusion of Cu cations into smaller pores. Interestingly, the opposite behavior was observed in our study (peak V), suggesting that zinc could not only retard the diffusion of Cu cations to 8-MR pores but also alter Cu cations to side pockets. Locations of Cu-Zn ion exchanges in mordenite were discussed by Reule et al. [30]. They used the Hartree-Fock-based quantum chemical calculations and DRIFTS analysis (the 12-MR/8-MR free Brønsted acid ratio) to demonstrate that Zn^{2+} is preferably exchanged in the 8-MR channels and side pockets. This may explain the hindering of Cu diffusion toward 8-MR pores when doping with Zn. The total H_2 consumption increased from 339.8 to 402.0 and 398.4 μmol/g-cat. when 0.5 and 1 wt% Zn were added, but decreased to 338.7 μmol/g-cat. when adding 3 wt% Zn. The increase of H_2 consumption of 0.5 and 1Zn/Cu-MOR samples could be attributed to Zn addition because the increased amounts of H_2 corresponded to the presence of peak IV. The similarity of both previous samples may be explained by the absence of Zn nanoparticles. Compared to 3 wt% Zn addition, a decrease of H_2 consumption was observed, implying the partial cover of Cu with ZnO_x species [35], which is suggested by XPS results in the next section.

1-3. X-ray Photoelectron Spectroscopy

The oxidation states of Cu and Zn were determined using XPS, as shown in Fig. 3. The spectra of Cu $2p_{3/2}$ and Zn $2p_{3/2}$ are illustrated in Fig. 3(a) and Fig. 3(b), respectively. The fitting of Cu $2p_{3/2}$ spectra exhibits three different peaks at 932.7, 934.2, and 936.3 eV, which correspond to Cu^+, isolated Cu^{2+}, and Cu^{2+} species bound to extra-framework oxygen (e.g., $Cu\text{-}OH^+$, mono and bis(μ-oxo) dicopper and tricopper sites), respectively [36]. The quantitative data of fitted results are summarized in Table 3. The Cu-MOR sample exhibits concentrations of Cu^+, isolated Cu^{2+} and Cu^{2+} species bound to extra-framework oxygen as 15.8, 62.9, and 21.3%,

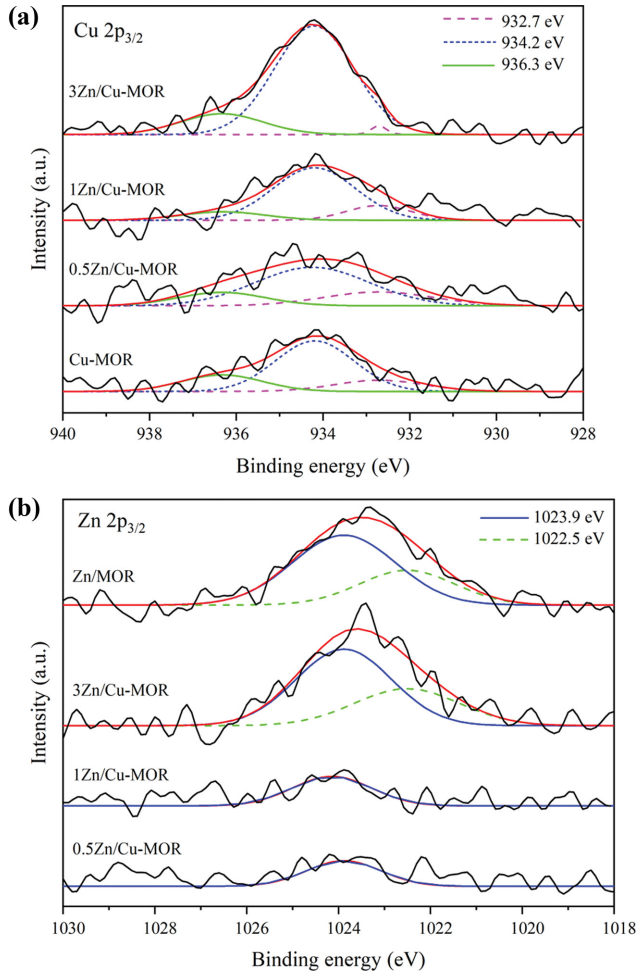

Fig. 3. Deconvolution of photoemission peaks of catalysts for the Cu $2p_{3/2}$ (a) and Zn $2p_{3/2}$ (b).

respectively. The total concentration of Cu^{2+} species is therefore 84.2%, which highly agrees with the concentration obtained from the H_2-TPR calculation result (81%). In the case of the Zn/Cu-MOR samples, concentrations of isolated Cu^{2+} significantly increase from 62.9 to 82.5%, while Cu^{2+} species bound to extra-framework oxygen from 21.3 to 16.2% with the increase of Zn to 3 wt%, indicating that Zn incorporation provides highly-dispersed Cu^{2+} species. Note that the increase of isolated Cu^{2+} species with Zn loading is in agreement with the significant rise of strong interaction features of Cu-Zn in the H_2-TPR profile (peak III and IV). This confirms that the effect of the strong interaction between Cu and Zn provides highly-dispersed Cu^{2+} species. In addition, 3Zn/Cu-MOR possesses the highest fraction of Cu^{2+} at 98.7%. However, the decrease of Cu^{2+} bound to extra-framework oxygen matches with the reduction of Cu^{2+} in the 12-MR pore (peak II).

The photoemission spectra of Zn $2p_{3/2}$ were fitted into peaks at 1,022.5 and 1,023.9 eV, as illustrated in Fig. 3(b). The peak at 1,022.5 eV could not be observed from 0.5 and 1Zn/Cu-MOR samples, but it was detected with 34.7 and 31.5 mol% of the total Zn from 3Zn/Cu-MOR and 3Zn/MOR samples. Niu et al. [37] reported that the binding energy peaks around 1,022.8 and 1,023.4 eV of Zn-impregnated HZSM-5 were attributed to the ZnO and $Zn(OH)^+$ species, respectively. The higher binding energy of ZnO-containing ZSM-5 compared with the bulk ZnO was owing to the higher electronegativity of oxygen in the zeolite framework [26]. Gong et al. [24] studied the ZnO modified ZSM-5 fabricated by atomic layer deposition (ALD). They demonstrated that the peak at 1,022.4 eV corresponds to the isolated $Zn(OH)^+$ species, which was the predominant form of the ZnO cluster based on the scheme of the ALD reaction. The reduction peak was also slightly higher than that of the reduction peak of nano ZnO. Gabrienko et al. [38] also prepared Zn^{2+}/BEA and ZnO/BEA by using solid-state exchange and ALD methods, which showed the XPS spectra at 1,023.3 and 1,022.8 eV. According to the EXAFS results and amount of Brønsted acid, they concluded that the peaks at 1,023.3 and 1,022.8 eV were attributed to Zn^{2+} cations in the cation exchange sites and -O-Zn-OH species. These species were a little bit larger than those of isolated O-$[Zn(OH)]^+$ species attached to the zeolite lattice, existing as a part of zinc oxide clusters. Therefore, it is reasonable to assign the peaks at 1,022.5 and 1,023.9 eV of our samples to the -O-Zn-OH species, which are precursors of very small ZnO clusters and Zn^{2+} bonded with lattice oxygen at the cation exchange sites, respectively. This demonstrates that -O-Zn-OH species increased with Zn loading, and this strengthened the existence of ZnO_x over layer Cu for 3Zn/Cu-MOR. In addition, the presence of Zn^{2+} at the exchange sites of a series Zn/Cu-MOR may explain the increase of isolated Cu^{2+} by the geometric effect that hinders the agglomeration of Cu clusters.

The Cu/Al molar ratio of Cu-MOR was 0.15 (Table 3), slightly lower than that obtained from ICP. When Zn was doped, the Cu/Al molar ratio monotonically increased to 0.19, 0.19, and 0.32 for 0.5, 1, and 3Zn/Cu-MOR, respectively. As the copper concentration of samples is based on a similar batch of Cu-MOR, confirmed by the Cu/Al ratio from ICP, which was relatively close, the

Table 3. Fitting result (%) of photoemission peaks of catalysts for the Cu $2p_{3/2}$ and Zn $2p_{3/2}$

Catalyst	Cu $2p_{3/2}$ (eV)			Zn $2p_{3/2}$ (eV)		Cu/Al molar ratio	Zn/Al molar ratio
	932.7	934.2	936.3	1,022.5	1,023.9		
Cu-MOR	15.8	62.9	21.3	n.d.	n.d.	0.15	-
0.5Zn/Cu-MOR	21.4	62.1	16.5	n.d.	100	0.19	0.06
1Zn/Cu-MOR	15.7	72.5	11.8	n.d.	100	0.19	0.07
3Zn/Cu-MOR	1.3	82.5	16.2	34.7	65.3	0.32	0.36
3Zn/MOR	n.d.	n.d.	n.d.	31.5	68.5	-	0.37

n.d. is not detected

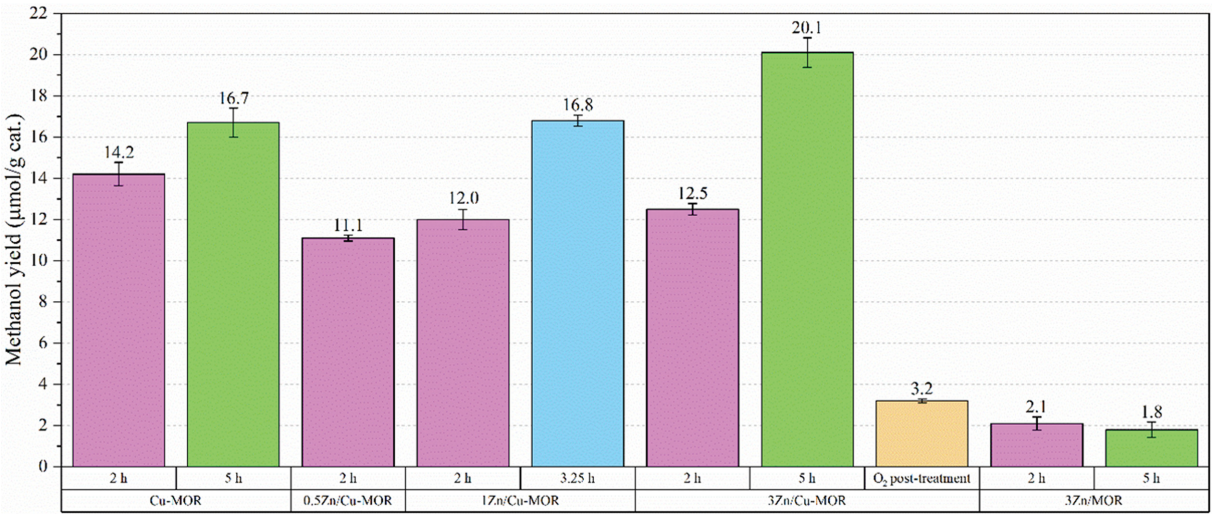

Fig. 4. Methanol yields of catalysts.

increase of Cu/Al molar ratio from the XPS result corresponded to the Cu surface enrichment [36]. However, the Zn/Al molar ratios are comparable to the result obtained from ICP, matching the H_2-TPR results that Zn^{2+} preferably exchanged in the 8-MR channels and side pockets. Thus, the result strengthens the effects of Zn on stabilizing highly-dispersed Cu^{2+} species and altering the location of Cu^{2+} from less-accessible pores to more-accessible pores and the external surface.

2. Reaction Study

Fig. 4 shows the methanol yield from the stepwise oxidation of methane for all samples. The methanol yield of Cu-MOR was 14.2± 0.57 μmol/g-cat. for methane loading of 2 h, which is comparable to the reported values in the range of 10-20 μmol/g-cat. for Cu-MOR (Si/Al=9-10) [21,39]. In the case of the Zn/Cu-MOR samples, methanol yields at 2 h of methane loading dropped to 11.1± 0.14, 12.0±0.49, and 12.5±0.28 μmol/g-cat. for 0.5Zn/Cu-MOR, 1Zn/Cu-MOR, and 3Zn/Cu-MOR, respectively. The decline of methanol yield at 2 h of methane loading for a series of Zn/Cu-MOR may be ascribed to the lower Cu^{2+} species bound to extra-framework oxygen (936.3 eV), which was proven to be the active site for this reaction by different research groups [40-42]. In situ XPS spectra in a study of Artiglia et al. clearly demonstrated that most of these species disappeared with the increase of Cu^{+} during methane loading [36].

However, if Cu^{2+} species bound to extra-framework oxygen were the only active sites (21.3%), it would be too low compared with the other Cu-containing MOR found in the literature [21,41,43]. Furthermore, we discovered that the colors of catalyst beds at 2 h of methane loading were different for each sample, as illustrated in Fig. 5(a)-(d). Fig. 5(a)-(b) displayed the color of O_2-activated Cu-MOR samples after methane loading at 30 min and 1 h. The color changed from dark blue into light blue with increasing duration of methane loading. Then, we increased the time of methane loading until the color of the entire bed was completely changed. The result showed that 1.5, 2, 3.25, and 5 h of methane loading was required for 0, 0.5, 1, and 3Zn/Cu-MOR samples, respectively. It is obvious that the completed methane loading time increased with

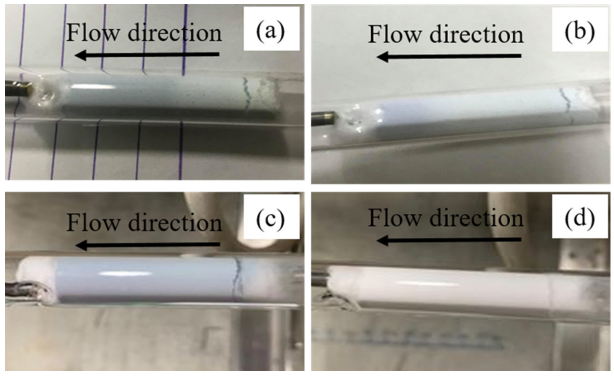

Fig. 5. Color change of catalysts (a)-(d); O_2-activated Cu-MOR after contact with methane for 30 min and 1 h (a), (b), O_2-activated 3Zn/Cu-MOR after contact with methane for 5 h followed with O_2 for 2 h (c), O_2-activated 3Zn/MOR after contact with methane for 2 h (d).

the increase of Zn. However, the change of active Cu^{2+} and methane-interacted Cu^{+} species during methane loading is still unclear [43].

Interestingly, higher methanol yields of Zn/Cu-MOR samples could be achieved when increasing methane loading time for 1Zn/Cu-MOR and 3Zn/Cu-MOR samples. It can be seen that 1Zn/Cu-MOR sample produced 16.8±0.27 μmol/g-cat. of methanol yield at only 3.25 h, which was very close to the 16.7±0.70 Cu-MOR sample at 5 h of methane loading time. Moreover, the methanol yield can be boosted up to 20.1±0.72 μmol/g-cat. from 3Zn/Cu-MOR sample, which was 20% higher than 16.7±0.70 μmol/g-cat. for Cu-MOR catalyst at a similar time (5 h) of methane loading (methanol yields of Cu-MOR and 3Zn/Cu-MOR at 5 h were performed in duplicate to confirm the reproducibility). 3Zn/MOR was also tested to strengthen the role of Zn on the enhancement of methanol yield, presenting that 3Zn/MOR produced methanol 2.1±0.32 and 1.8±0.37 μmol/g-cat. at 2 and 5 h. This confirms that the higher yield of 3Zn/Cu-MOR at 5 h was not attributed to the individual Cu and Zn but the synergy of bimetallic Cu-ZnO_x. Again, it should be noted that the participation of isolated Cu^{2+}

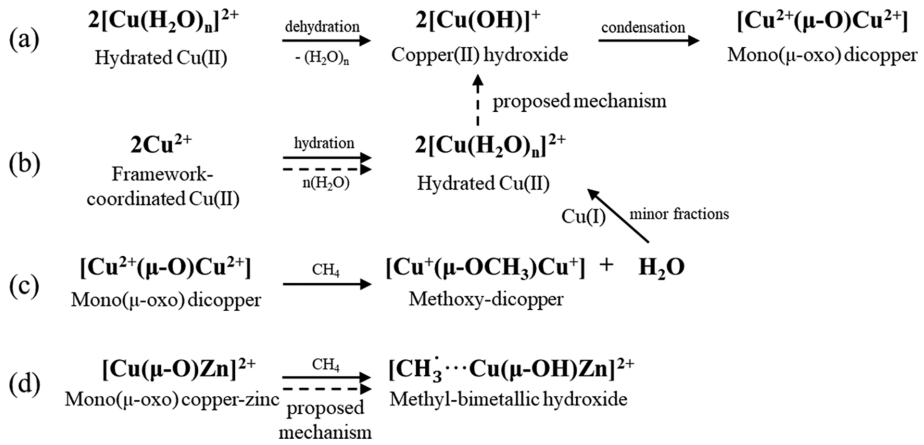

Schematic 1. Mechanisms of formation of mono(μ-oxo) dicopper (a), hydrolysis of framework-coordinated Cu^{2+} to hydrated-Cu^{2+} (b), formation of minor fractions of hydrated-Cu^{2+} during interaction of the O_2-activated Cu-MOR with methane (c), methane activation on bimetallic mono(μ-oxo) copper-zinc (d).

species (934.2 eV) in the reaction was clearly observed during methane loading of the second cycle [36]. The in situ XPS spectra revealed that a significant fraction of isolated Cu^{2+} species reduced with the increase of Cu^{+}. Therefore, it is reasonable to propose that isolated Cu^{2+} species can be a precursor for active Cu species during exposure to methane.

It is widely accepted that the active μ-oxo bridges between Cu^{2+} species, formed by the condensation of two adjacent $[Cu(OH)]^{+}$ species, is generated from the dehydration of $[Cu(H_2O)_n]^{2+}$ during thermal treatment [42,44] as illustrated in Schematic 1(a). Lomachenko et al. [43] described the reverse mechanism that some of the framework-coordinated Cu^{2+} species immediately hydrolyzed to pseudo-octahedral Cu^{2+} aquo complexes (hydrated-Cu^{2+}) when steam is admitted (extraction step) as shown in Schematic 1(b). Moreover, they also observed minor fractions of hydrated-Cu^{2+} during interaction of the O_2-activated material with methane, suggesting that small quantities of water might have been produced together with methoxy-dicopper before the generated water slowly interacted with Cu(I), as expressed in Schematic 1(c). The methoxy species can be extracted as methanol and the Cu-O-Cu can be regenerated with the help of water [1]. Copper(II) hydroxide was also proven to be the active site with less activity compared to the mono and bis(μ-oxo) dicopper [36,45]. This may explain the reason for the higher methanol yield of 3Zn/Cu-MOR, owing to the hydration of highly-dispersed Cu^{2+} toward active Cu^{2+} species ($[Cu(OH)]^{+}$ and $[Cu^{2+}(\mu\text{-O})Cu^{2+}]$) during methane loading through the proposed mechanism in Schematic 1(b). Furthermore, $[Cu(\mu\text{-O})Zn]^{2+}$ bimetallic center in ZSM-5 zeolite exhibited a higher barrier for methane activation than $[Cu(\mu\text{-O})Cu]^{2+}$ monometallic center, as illustrated in Schematic 1(d) [46]. The CH_3 radical can further react with the neighbor OH group, resulting in the product complex. This also describes the requirement for a longer methane loading time for 3Zn/Cu-MOR. The proposed mechanisms demonstrate the role of Zn on active Cu species for the stepwise oxidation of methane to methanol, leading to an increase in methanol yield per cycle.

According to Gabrienko et al. [20], Zn-exchanged mordenite can activate gas-phase methane to adsorb methyl species, which can be converted to methoxy species with O_2 contact, suggesting that Zn^{2+} could be active sites for partial oxidation of methane into methanol. Therefore, we also tested our superior catalyst, 3Zn/Cu-MOR, by further treating the methane-saturated 3Zn/Cu-MOR (5 h) with O_2 at 200 °C for 2 h. The result showed that the methanol yield was reduced from 20.1±0.72 to 3.2±0.1 μmol/g-cat. This suggests that copper might promote the over-oxidation of methyl species, as seen in Fig. 5(c) of which color of the catalyst is back to dark blue. Fig. 5(d) displays the color of 3Zn/MOR after loading methane for 2 h (white), and the change during contact with methane could not be observed.

CONCLUSION

XRD and N_2-physisorption results confirmed that the addition of Zn inconsiderably changed the structure of mordenite zeolite, highlighting the effects of Zn on active Cu species and their locations for the stepwise oxidation of methane into methanol. The H_2-TPR and XPS measurements demonstrated that the addition of Zn led to the formation of the strong interaction between Cu and ZnO_x, resulting in highly dispersed Cu^{2+} at more accessible locations in 12-MR and 8-MR side pocket. This highly dispersed Cu^{2+} can be attributed to the precursor for active Cu^{2+} species due to the transformation to active Cu^{2+} species during methane loading. In addition, the bimetallic Cu-ZnO_x center is also able to activate methane, although it has a slower rate than monometallic Cu. Therefore, 3Zn/Cu-MOR produced a lower methanol yield than Cu-MOR at 2 but 20%-higher methanol yield at 5 h of methane loading time. This work demonstrates the advantage of strong Cu-ZnO_x interaction for the stepwise oxidation of methane to methanol by stabilizing highly dispersed Cu^{2+} sites.

ACKNOWLEDGEMENTS

This work was supported by Thailand Science Research and Innovation (formerly Thailand Research Fund) and Office of the Higher Education Commission of Thailand [grant numbers MRG6

280224] and Silpakorn University Research, Innovation and Creative Fund.

DECLARATION OF INTEREST

There is no conflict of interest to declare.

REFERENCES

1. V. L. Sushkevich, D. Palagin, M. Ranocchiari and J. A. van Bokhoven, *Science*, **356**, 523 (2017).
2. C. Elvidge, M. Zhizhin, K. Baugh, F.-C. Hsu and T. Ghosh, *Energies*, **9**, 14 (2015).
3. S. H. Lee, J. K. Kang and E. D. Park, *Korean J. Chem. Eng.*, **35**, 2145 (2018).
4. P. Tang, Q. Zhu, Z. Wu and D. Ma, *Energy Environ. Sci.*, **7**, 2580 (2014).
5. M. Ren, Q. Shi, L. Mi, W. Liang, M. Yuan, L. Wang, Z. Gao, W. Huang, J. Huang and Z. Zuo, *Mater. Today Sustain.*, **11-12**, 100061 (2021).
6. R. Balasubramanian, S. M. Smith, S. Rawat, L. A. Yatsunyk, T. L. Stemmler and A. C. Rosenzweig, *Nature*, **465**, 115 (2010).
7. M. Merkx, D. A. Kopp, M. H. Sazinsky, J. L. Blazyk, J. Müller and S. J. Lippard, *Angew. Chem. Int. Ed.*, **40**, 2782 (2001).
8. M. H. Groothaert, P. J. Smeets, B. F. Sels, P. A. Jacobs and R. A. Schoonheydt, *J. Am. Chem. Soc.*, **127**, 1394 (2005).
9. E. Mae Alayon, M. Nachtegaal, M. Ranocchiari and J. A. Van Bokhoven, *Chem. Commun.*, **48**, 404 (2012).
10. K. Narsimhan, K. Iyoki, K. Dinh and Y. Román-Leshkov, *ACS Cent. Sci.*, **2**, 424 (2016).
11. S. Grundner, M. A. C. Markovits, G. Li, M. Tromp, E. A. Pidko, E. J. M. Hensen, A. Jentys, M. Sanchez-Sanchez and J. A. Lercher, *Nat. Commun.*, **6**, 1 (2015).
12. R. Arvaneh, A. A. Fard, A. Bazyari, S. M. Alavi and F. J. Abnavi, *Korean J. Chem. Eng.*, **36**, 1033 (2019).
13. N. Chotigkrai, Y. Hochin, J. Panpranot and P. Praserthdam, *React. Kinet. Mech. Catal.*, **117**, 565 (2016).
14. P. Tomkins, A. Mansouri, V. L. Sushkevich, L. I. Van der Wal, S. E. Bozbag, F. Krumeich, M. Ranocchiari and J. A. Van Bokhoven, *Chem. Sci.*, **10**, 167 (2019).
15. H. Geng, Z. Yang, L. Zhang, J. Ran and Y. Yan, *Energy Convers. Manag.*, **132**, 339 (2017).
16. Y. Zhao, B. Shan, Y. Wang, J. Zhou, S. Wang and X. Ma, *Ind. Eng. Chem. Res.*, **57**, 4526 (2018).
17. M. Behrens, F. Studt, I. Kasatkin, S. Kühl, M. Hävecker, F. Abild-Pedersen, S. Zander, F. Girgsdies, P. Kurr, B. L. Kniep, M. Tovar, R. W. Fischer, J. K. Nørskov and R. Schlögl, *Science*, **336**, 893 (2012).
18. W. Qi, Q. Ling, D. Ding, C. Yazhong, S. Chengwu, C. Peng, W. Ye, Z. Qinghong, L. Rong and S. Hao, *Catal. Commun.*, **108**, 68 (2018).
19. A. A. C. Reule and N. Semagina, *ACS Catal.*, **6**, 4972 (2016).
20. A. A. Gabrienko, S. S. Arzumanov, M. V. Luzgin, A. G. Stepanov and V. N. Parmon, *J. Phys. Chem. C*, **119**, 24910 (2015).
21. H. V. Le, S. Parishan, A. Sagaltchik, C. Göbel, C. Schlesiger, W. Malzer, A. Trunschke, R. Schomäcker and A. Thomas, *ACS Catal.*, **7**, 1403 (2017).
22. T. Zhou, L. Li, C. Jie, Q. Shen, Q. Xie and Z. Hao, *Ceram. Int.*, **35**, 3097 (2009).
23. D. Zhang, H. Zhang and Y. Yan, *Micropor. Mesopor. Mater.*, **243**, 193 (2017).
24. T. Gong, L. Qin, J. Lu and H. Feng, *Phys. Chem. Chem. Phys.*, **18**, 601 (2016).
25. K. Narsimhan, K. Iyoki, K. Dinh and Y. Román-Leshkov, *ACS Cent. Sci.*, **2**, 424 (2016).
26. S. Tamiyakul, W. Ubolcharoen, D. N. Tungasmita and S. Jongpatiwut, *Catal. Today*, **256**, 325 (2015).
27. A. A. C. Reule, J. Shen and N. Semagina, *ChemPhysChem*, **19**, 1500 (2018).
28. A. Sainz-Vidal, J. Balmaseda, L. Lartundo-Rojas and E. Reguera, *Micropor. Mesopor. Mater.*, **185**, 113 (2014).
29. P. Vanelderen, J. Vancauwenbergh, M.-L. Tsai, R. G. Hadt, E. I. Solomon, R. A. Schoonheydt and B. F. Sels, *ChemPhysChem*, **15**, 91 (2014).
30. A. A. C. Reule, V. Prasad and N. Semagina, *Micropor. Mesopor. Mater.*, **263**, 220 (2018).
31. Z. Fu, D. Yin, Y. Yang and X. Guo, *Appl. Catal. A, Gen.*, **124**, 59 (1995).
32. A. G. Popov, A. V. Smirnov, E. E. Knyazeva, V. V. Yuschenko, E. A. Kalistratova, K. V. Klementiev, W. Grünert and I. I. Ivanova, *Micropor. Mesopor. Mater.*, **134**, 124 (2010).
33. T. Lunkenbein, J. Schumann, M. Behrens, R. Schlögl and M. G. Willinger, *Angew. Chem. Int. Ed.*, **54**, 4544 (2015).
34. R. Dalebout, N. L. Visser, C. E. L. Pompe, K. P. de Jong and P. E. de Jongh, *J. Catal.*, **392**, 150 (2020).
35. Q. Liu, Z. Zhao, M. Arai, C. Zhang, K. Liu, R. Shi, P. Wu, Z. Wang, W. Lin, H. Cheng and F. Zhao, *Catal. Sci. Technol.*, **10**, 4412 (2020).
36. L. Artiglia, V. L. Sushkevich, D. Palagin, A. J. Knorpp, K. Roy and J. A. Van Bokhoven, *ACS Catal.*, **9**, 6728 (2019).
37. X. Niu, J. Gao, Q. Miao, M. Dong, G. Wang, W. Fan, Z. Qin and J. Wang, *Micropor. Mesopor. Mater.*, **197**, 252 (2014).
38. A. A. Gabrienko, S. S. Arzumanov, A. V. Toktarev, I. G. Danilova, I. P. Prosvirin, V. V. Kriventsov, V. I. Zaikovskii, D. Freude and A. G. Stepanov, *ACS Catal.*, **7**, 1818 (2017).
39. M. A. Newton, A. J. Knorpp, V. L. Sushkevich, D. Palagin and J. A. Van Bokhoven, *Chem. Soc. Rev.*, **49**, 1449 (2020).
40. A. R. Kulkarni, Z. J. Zhao, S. Siahrostami, J. K. Nørskov and F. Studt, *ACS Catal.*, **6**, 6531 (2016).
41. D. K. Pappas, A. Martini, M. Dyballa, K. Kvande, S. Teketel, K. A. Lomachenko, R. Baran, P. Glatzel, B. Arstad, G. Berlier, C. Lamberti, S. Bordiga, U. Olsbye, S. Svelle, P. Beato and E. Borfecchia, *J. Am. Chem. Soc.*, **140**, 15270 (2018).
42. T. Ikuno, S. Grundner, A. Jentys, G. Li, E. Pidko, J. Fulton, M. Sanchez-Sanchez and J. A. Lercher, *J. Phys. Chem. C*, **123**, 8759 (2019).
43. K. A. Lomachenko, A. Martini, D. K. Pappas, C. Negri, M. Dyballa, G. Berlier, S. Bordiga, C. Lamberti, U. Olsbye, S. Svelle, P. Beato and E. Borfecchia, *Catal. Today*, **336**, 99 (2019).
44. E. M. C. Alayon, M. Nachtegaal, A. Bodi, M. Ranocchiari and J. A. Van Bokhoven, *Phys. Chem. Chem. Phys.*, **17**, 7681 (2015).
45. J. Meyet, A. Ashuiev, G. Noh, M. A. Newton, D. Klose, K. Searles, A. P. van Bavel, A. D. Horton, G. Jeschke, J. A. van Bokhoven and C. Copéret, *Angew. Chem. Int. Ed.*, **60**, 16200 (2021).
46. G. Wang, L. Huang, W. Chen, J. Zhou and A. Zheng, *Phys. Chem. Chem. Phys.*, **20**, 26522 (2018).